The Journal of Chemical Physics

RESEARCH ARTICLE | NOVEMBER 03 2026

Vibrational spectra and anharmonic coupling of the O–H stretch in 10-hydroxybenzo[h]quinoline: Insights from constrained nuclear–electronic orbital theory

Hypatia K. Newton ; Yiwen Wang ; Yang Yang

Check for updates

J. Chem. Phys. 165, 174310 (2026)
https://doi.org/10.1063/5.0358420
CHORUS

View Online
Export Citation

Articles You May Be Interested In

The constrained nuclear–electronic orbital (CNEO) framework for nuclear quantum effects in quantum chemistry and molecular simulations

APL Computational Physics (April 2026)

Excited-state intramolecular proton transfer dynamics with neural network potentials and nuclear quantum effects

J. Chem. Phys. (November 2026)

Molecular reorganization of selected quinoline derivatives in the ground and excited states—Investigations via static DFT

J. Chem. Phys. (July 2015)

12 November 2026 14:28:20

AIP Publishing

AIP Publishing
The Journal of Chemical Physics
Special Topics Open for Submissions
Learn More

The Journal of Chemical Physics ARTICLE pubs.aip.org/aip/jcp

Vibrational spectra and anharmonic coupling of the O–H stretch in 10-hydroxybenzo[h]quinoline: Insights from constrained nuclear–electronic orbital theory

Cite as: J. Chem. Phys. 165, 174310 (2026); doi: 10.1063/5.0358420
Submitted: 28 August 2026 • Accepted: 16 October 2026 •
Published Online: 3 November 2026

View Online Export Citation CrossMark

Hypatia K. Newton, Yiwen Wang, and Yang Yang[a)]

AFFILIATIONS

Theoretical Chemistry Institute and Department of Chemistry, University of Wisconsin-Madison, 1101 University Avenue, Madison, Wisconsin 53706, USA

[a)]Author to whom correspondence should be addressed: yyang222@wisc.edu

ABSTRACT

Hydrogen bonds can exhibit pronounced nuclear quantum effects (NQEs) that strongly influence proton-transfer dynamics. 10-hydroxybenzo[h]quinoline (HBQ) is a prototypical excited-state intramolecular proton transfer (ESIPT) system with a strong intramolecular hydrogen bond, and its vibrational spectra and anharmonic mode couplings have recently attracted considerable interest. Here, we use constrained nuclear–electronic orbital density functional theory (CNEO-DFT) and molecular dynamics (CNEO-MD), which account for NQEs, particularly nuclear quantum delocalization effects, to investigate the O–H stretching vibration (ν_{OH}) of HBQ and its anharmonic coupling with other modes in the ground state. The ν_{OH} frequency calculated by CNEO-DFT agrees closely with the experiment, and CNEO-MD reproduces the characteristic finger-like structure of the infrared spectrum. Normal mode frequency shift analysis and CNEO-MD simulations with resonant ν_{OH} excitation consistently identify several low-frequency in-plane backbone bending modes that are strongly coupled to the ν_{OH}. Taken together, this work establishes a detailed understanding of the ground-state vibrational spectrum and ν_{OH} mode couplings in HBQ, providing a basis for further investigation of their roles in ESIPT dynamics.

Published under an exclusive license by AIP Publishing. https://doi.org/10.1063/5.0358420

12 November 2026 14:28:20

I. INTRODUCTION

Proton transfer is a fundamental chemical transformation where a hydrogen nucleus is transferred from a donor site to an acceptor site. Excited-state intramolecular proton transfer (ESIPT) is a distinctive proton-transfer process that typically happens after photoexcitation. It often features fast excited-state relaxation, a large Stokes shift, and strong sensitivity to hydrogen bonding,[1–4] which makes ESIPT systems promising for a wide range of applications, including fluorescence markers for bioimaging,[4,5] optoelectronics,[6] and solar concentrators.[7]

ESIPT dynamics are often highly sensitive to skeletal motions, which can contract the donor–acceptor distance and reshape the proton-transfer potential, thereby influencing proton transfer dynamics.[8–14] Therefore, understanding and rationally tuning ESIPT behavior requires a detailed understanding of how hydrogen-bond structure and vibrational dynamics affect the proton transfer process.

As a prototypical ESIPT system, 10-hydroxybenzo[h]quinoline (HBQ) contains a strong intramolecular hydrogen bond and undergoes ultrafast proton transfer upon photoexcitation (Fig. 1).[8,14–18] The proton transfer dynamics are highly sensitive to the intramolecular hydrogen bond geometry and the distance between the oxygen and nitrogen atoms, which are directly related to and can be manifested in the O–H stretching vibration (ν_{OH}) frequency.[19–23] Therefore, the characterization of the ν_{OH} vibration in HBQ as well as its anharmonic coupling to the skeletal vibrations that modulate the oxygen–nitrogen distance has been a focus of recent experimental and theoretical studies.[8,14,24–27] Studies from the Khalil group using ultrafast pump–probe spectroscopy identified two

Published under an exclusive license by AIP Publishing

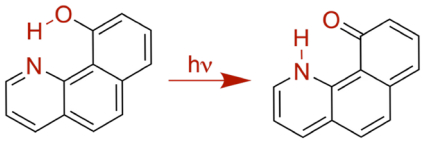


FIG. 1. Structure of HBQ, which undergoes ESIPT upon photoexcitation.

specific low-frequency modes that may participate in this coupling,[24,25] and later work by the Xiong group used density functional theory (DFT)-based anharmonic vibrational analysis and found several additional candidates.[26] However, no definitive conclusions have been achieved, and it is unclear yet whether coupling to the ν_{OH} is dominated by a small number of low-frequency modes or distributed across a broader range of modes. Resolving these questions is necessary to understand the role of the skeletal motions and how they can promote or inhibit ESIPT dynamics.

In addition, another unsolved question concerns the infrared (IR) spectrum of HBQ, which was observed to give a broadband with a finger-like structure in the ν_{OH} region.[24] Previous theoretical work assigns the observed peaks to coupling between the fundamental and four low-frequency modes,[26] three of which are in-plane backbone motions that modulate the oxygen–nitrogen distance, and one of which is not. This interesting observation motivates us to reexamine the peak assignments and mode couplings that can potentially give rise to the band structure.

Characterizing the ν_{OH} and its anharmonic couplings with other modes requires an accurate treatment of the proton. Because of the light mass of the proton, nuclear quantum effects (NQEs), particularly zero-point energy (ZPE) and nuclear quantum delocalization, can substantially influence the O–H bond length, donor–acceptor distance, and associated vibrational frequencies and spectra.[28–30] Therefore, a reliable characterization of mode couplings in HBQ requires a method that can explicitly incorporate NQEs.

Existing methods to incorporate NQEs, such as multiconfiguration time-dependent Hartree,[31] vibrational self-consistent field theory,[32,33] and path integral methods,[34–36] are often computationally expensive for *ab initio* calculations for a molecule as large as HBQ. Recently, our group has developed the constrained nuclear–electronic orbital (CNEO) framework, which provides an efficient alternative for incorporation of NQEs, particularly nuclear quantum delocalization effects, into quantum chemistry calculations and *ab initio* molecular dynamics (AIMD).[37–41] The framework has already proven useful for studying hydrogen-related dynamics and kinetics,[42,43] vibrational spectra,[40,44–48] and nonadiabatic dynamics.[49] In addition, extensions to the CNEO framework, including CNEO with the implicit solvent model,[50] CNEO QM/MM,[51] and periodic CNEO theory,[52,53] have enabled efficient and accurate simulation of hydrogen-related processes in more complex environments.

In this work, we apply constrained nuclear–electronic orbital density functional theory (CNEO-DFT) and molecular dynamics (CNEO-MD) to investigate the ν_{OH} vibrational spectrum and its anharmonic couplings in HBQ. In particular, we assess how the inclusion of NQEs through the CNEO framework affects the equilibrium structure, harmonic vibrational frequencies, and simulated vibrational spectrum by comparing results obtained from conventional and CNEO methods. We then perform both normal mode frequency shift analysis and CNEO-MD with resonant electric field excitation to identify the modes coupled to ν_{OH}. Our results show that the inclusion of NQEs through the CNEO framework significantly improves the accuracy of vibrational frequency and spectrum predictions, and they reveal clear coupling between ν_{OH} and a set of low-frequency modes that are in-plane backbone bending motions that directly modulate the intramolecular hydrogen bond distance.

This paper is organized as follows: Sec. II briefly introduces the CNEO framework. Section III provides the computational details. Section IV presents a comparison of the equilibrium geometry and vibrational spectrum of HBQ calculated using conventional and CNEO methods, followed by an analysis of anharmonic mode couplings of the ν_{OH} in HBQ. Section V details the conclusions.

II. METHODS

A. CNEO framework

The CNEO framework extends multicomponent quantum chemistry, in which both electrons and nuclei are treated quantum mechanically.[54–59] In conventional multicomponent quantum chemistry, quantum nuclear wave functions optimize freely for each set of classical nuclear coordinates, so only reduced-dimension potential energy surfaces (PESs) can be defined, and quantum nuclei are not directly tied to conventional molecular geometries. On the reduced-dimension PESs, dynamics are highly nonadiabatic and are computationally expensive to perform.[41] The CNEO framework resolves this challenge and reestablishes full-dimensional effective PESs by constraining the position expectation value of each quantum nucleus to correspond to classical coordinates,

$$\langle \boldsymbol{R}_I \rangle = \boldsymbol{R}_I^{\mathrm{geo}}, \tag{1}$$

where $\langle \boldsymbol{R}_I \rangle$ is the position expectation value of the I-th quantum nucleus and $\boldsymbol{R}_I^{\mathrm{geo}}$ is the corresponding designated classical position.[37,38] This treatment relies on the distinguishable particle assumption, which is justified by the physical fact that in most chemical systems of interest, nuclei remain significantly localized with essentially no overlap, allowing them to be treated as distinguishable particles with well-defined position expectation values.

In CNEO-DFT, the constrained multicomponent Kohn–Sham equations are obtained by minimizing the total energy with respect to both the nuclear orbitals ($\{\phi_I^{\mathrm{n}}\}$) and the electronic orbitals ϕ^{e} subject to the constraints in Eq. (1),[37]

$$\left(-\frac{1}{2}\nabla^2 + v^{\mathrm{e}}\right)\phi^{\mathrm{e}} = \varepsilon^{\mathrm{e}}\phi^{\mathrm{e}}, \tag{2}$$

$$\left(-\frac{1}{2m_I^{\mathrm{n}}}\nabla^2 + v_I^{\mathrm{n}} + \boldsymbol{f}_I^{\mathrm{n}} \cdot \left(\boldsymbol{R}_I - \boldsymbol{R}_I^{\mathrm{geo}}\right)\right)\phi_I^{\mathrm{n}} = \varepsilon_I^{\mathrm{n}}\phi_I^{\mathrm{n}}. \tag{3}$$

Here, we use superscripts e and n to denote the electrons and nuclei, respectively, and I to index the nuclei. m^{n} denotes the nuclear mass and ε denotes the multicomponent Kohn–Sham orbital energy. The electronic and nuclear Kohn–Sham equations each consist of a kinetic energy operator (∇^2) and an effective electronic or nuclear potential (v^{e} or v^{n}). $\boldsymbol{f}_I^{\mathrm{n}}$ is the Lagrange multiplier enforcing the

12 November 2026 14:28:20

Published under an exclusive license by AIP Publishing

expectation position constraint on the I-th quantum nucleus, creating the additional $f_I^{\mathrm{n}} \cdot \left(\boldsymbol{R}_I - \boldsymbol{R}_I^{\mathrm{geo}}\right)$ term in the nuclear equation. Solving the coupled equations self-consistently while enforcing the nuclear position constraints provides the multicomponent ground-state orbitals, orbital energies, and the CNEO-DFT total energy. Since the CNEO energy depends on both the constrained position expectation values of the quantum nuclei and the coordinates of the classical nuclei, it essentially defines an effective PES with nuclear quantum delocalization effects incorporated.[37,38,41]

In CNEO-MD, the nuclear position expectation values are propagated classically on the CNEO effective PES. With an adiabatic approximation, the equations of motion for the quantum nuclei are as follows:[40,60]

$$m\frac{\mathrm{d}\langle \boldsymbol{R}\rangle}{\mathrm{d}t} = \langle \boldsymbol{P}\rangle, \tag{4}$$

$$\frac{\mathrm{d}\langle \boldsymbol{P}\rangle}{\mathrm{d}t} = -\nabla_{\langle \boldsymbol{R}\rangle} V_{\mathrm{CNEO}}(\langle \boldsymbol{R}\rangle), \tag{5}$$

where $\langle \boldsymbol{R}\rangle$ and $\langle \boldsymbol{P}\rangle$ are the expectation values of nuclear position and momentum operators, respectively, m is the nuclear mass, and $V_{\mathrm{CNEO}}(\langle \boldsymbol{R}\rangle)$ is the CNEO effective PES. For the propagation of classical nuclei, the equations of motion are the same except that the expectation values of position and momentum, $\langle \boldsymbol{R}\rangle$ and $\langle \boldsymbol{P}\rangle$, are replaced with classical position and momentum, $\boldsymbol{R}$ and $\boldsymbol{P}$. These equations are almost identical to those of conventional AIMD, except for the CNEO effective PES in place of the conventional DFT surface. The CNEO framework leads to a small increase in computational cost (typically less than 15%),[45] while often providing substantial improvements in structures and dynamics.[40,44–47]

III. COMPUTATIONAL DETAILS

All DFT and CNEO-DFT calculations were performed using a locally modified version of PySCF,[61,62] available on our group's GitHub repository.[63] The geomeTRIC package interfaced through PySCF was used for geometry optimization.[64] AIMD and CNEO-MD simulations were carried out using the Atomic Simulation Environment (ASE).[65] Visualization was assisted by Jmol[66] and VMD.[67] Anharmonic vibrational frequencies were also calculated using second-order vibrational perturbation theory (VPT2)[68,69] in Gaussian 16[70] using the deperturbed VPT2 (DVPT2)[71] treatment.

For all calculations, we employed the B3LYP functional and the def2-TZVP electronic basis set. This functional and basis set were chosen based on benchmarking the harmonic frequency analysis for HBQ. We tested the B3LYP,[72–74] PBE0,[75] and ωB97M-V[76] functionals and def2-TZVP,[77] def2-TZVPP,[77] and aug-cc-pVDZ[78] electronic basis sets (see the supplementary material). For each functional-basis combination, DFT and CNEO-DFT geometries were optimized separately at the corresponding level of theory prior to harmonic frequency analysis. In earlier work by our group, benchmarking results compared to CCSD(T) results were often used to determine the best functional and basis set for a given system.[40,42–45] Unfortunately, CCSD(T) is highly expensive for the large HBQ molecule, and the same benchmarking is not viable. However, among the tested methods, CNEO-B3LYP/def2-TZVP gave one of the closest ν_{OH} frequency predictions to experiment, and thus this functional-basis combination is used throughout this work. While this choice is motivated empirically, as we discuss in the supplementary material, most other basis sets and functionals would not qualitatively alter the results obtained by CNEO and conventional DFT. In CNEO calculations, all protons were treated quantum mechanically using the PB4-D basis set,[79] and all other nuclei were treated as classical point charges. No electron–proton correlation functional was used in the CNEO calculations, as previous benchmark tests suggest that existing electron–proton correlation functionals do not make a qualitative difference to vibrational spectra.[80]

Vibrational spectra were calculated both by harmonic analysis and from MD simulations. The MD simulations were conducted in the microcanonical ensemble with energy-equipartition presets, denoted as *NVE*-eqp.[44] In this protocol, multiple *NVE* simulations are initiated from the optimized geometry, with kinetic energy of k_BT assigned to each normal mode and velocity directions randomly chosen, where k_B is the Boltzmann constant and T is the assigned temperature. For each T, 50 trajectories of length 2 ps were simulated. IR spectra were then obtained by Fourier transforming the dipole derivative autocorrelation function and averaging over the 50 trajectories at each simulation T. Convergence tests (see the supplementary material) show that the main spectral features and peak positions are largely converged with this ensemble size of 50, although the intensities of fine-structure peaks still show some remaining dependence on the number of trajectories.

Normal mode frequency shift analysis[81] was performed to assess how the displacement of each normal mode affects the ν_{OH} frequency. In this analysis, each mode was approximated as a harmonic oscillator, and the displacement amplitude A was chosen to satisfy $k_BT = \frac{1}{2}m_{\mathrm{eff}}\omega^2A^2$, where T is a temperature parameter and is set to 300 K in this work, and m_{eff} and ω are the effective mass and angular frequency of the mode, respectively. The optimized geometry was displaced along each normal mode in both positive and negative directions, and mode frequencies were recalculated by diagonalizing the numerical Hessian matrix evaluated at each displaced geometry. The effect of displacement along a normal mode i on the ν_{OH} frequency was quantified as $\Delta\nu_{(\mathrm{OH},i)} = \nu_{(\mathrm{OH})}\left(\boldsymbol{R}_{(i,\mathrm{disp})}\right) - \nu_{(\mathrm{OH})}\left(\boldsymbol{R}_{(\mathrm{opt})}\right)$, where $\boldsymbol{R}_{(i,\mathrm{disp})}$ is the geometry displaced along normal mode i, $\boldsymbol{R}_{(\mathrm{opt})}$ is the optimized geometry, and $\Delta\nu_{(\mathrm{OH},i)}$ is the resulting shift in the ν_{OH} frequency. Since each normal mode can have two displacement directions, we separately calculated the frequency shift for each direction and averaged over the absolute value of the shift. Larger values of the average $\left|\Delta\nu_{(\mathrm{OH},i)}\right|$ generally suggest stronger coupling between mode i and the ν_{OH}.

To investigate mode-specific vibrational couplings, we also classically mimic an ultrafast pump pulse by applying a time-dependent oscillating electric field during CNEO-MD, using the electric-field response implemented previously within the CNEO framework.[48] The electric field was applied in the initial direction of the O–H bond and oscillated at the frequency of the ν_{OH} to resonantly excite the ν_{OH}. The electric field was modulated by a Gaussian to more closely mimic wave packet excitation, and it was applied for 40 fs to match the length of the experimental pump pulse used to excite the ν_{OH} in HBQ.[24] Multiple electric field strengths were tested to achieve a final ν_{OH} energy of approximately one quantum of vibrational energy.

12 November 2026 14:28:20

Published under an exclusive license by AIP Publishing

With the electric field excitation, modes that couple with the excited ν_{OH} gain energy from the intramolecular vibrational redistribution. Time evolutions of these mode-specific energies were extracted using mode coefficient decomposition, as described in the supplementary material.

IV. RESULTS AND DISCUSSION

A. Geometry

Figure 2 shows the optimized ground-state structure of HBQ using both conventional DFT and CNEO-DFT. Compared to DFT, which predicts an O–H distance of 0.99 Å and an N···H distance of 1.71 Å, CNEO-DFT predicts a longer O–H bond length of 1.03 Å and a shorter N···H distance of 1.64 Å. This difference is due to the change in the effective PES for the proton with the inclusion of nuclear quantum delocalization effects, which shifts the proton toward the nitrogen atom and forms a stronger intramolecular hydrogen bond. This result is consistent with past CNEO studies showing strengthened hydrogen bonding and enhanced proton sharing in previously studied hydrogen-bonded systems.[43,45,46,51]

B. Vibrational spectra

At each optimized geometry, we performed harmonic analysis and obtained the normal mode frequencies. Comparison of the ν_{OH} frequency obtained from conventional DFT and CNEO-DFT reveals a substantial effect from NQEs (Table I). DFT predicts a ν_{OH} frequency of 3148 cm^{-1}, significantly higher than the experimental band centered around 2750 cm^{-1}.[24–26] This significant overestimation of the ν_{OH} is observed for all tested functionals and basis sets. Only after anharmonic correction is the accurate ν_{OH} frequency obtained, as DVPT2 significantly lowers the ν_{OH} frequency from 3148 to 2788 cm^{-1}. CNEO-DFT harmonic analysis predicts the ν_{OH} frequency to be 2771 cm^{-1}, which differs from the experimental value by 21 cm^{-1} and is in close agreement with DVPT2. Notably, close agreement between VPT2 methods and CNEO-DFT has been observed previously,[39,46] despite their fundamentally different treatments of anharmonicity: VPT2 accounts for anharmonic effects perturbatively on the conventional DFT PES, whereas in CNEO-DFT, nuclear quantum delocalization modifies the underlying effective PES on which harmonic analysis is performed. We also note that this improvement of CNEO-DFT over conventional DFT is consistent across all tested functionals and basis sets, as shown by extensive benchmark tests provided in the supplementary material. Interestingly, although in the past the ωB97M-V functional was often chosen as a reliable functional for describing hydrogen-bonded interactions,[47,82,83] it predicts ν_{OH} frequencies ~200 cm^{-1} higher than those predicted by the PBE0 and B3LYP functionals, for both conventional DFT and CNEO-DFT. We leave the reason for this unusual behavior of the ωB97M-V functional to be investigated in future work. The lower frequency prediction of the ν_{OH} using CNEO-DFT can be rationalized by the stronger hydrogen-bond interaction, and thus a weaker O–H bond. This is consistent with past studies, where NQEs captured by the CNEO framework significantly influence both the structure and vibrational spectrum of hydrogen-bonded systems.[44–47]

TABLE I. Calculated ν_{OH} frequency using DFT, DVPT2, and CNEO-DFT. DFT overestimates the experimental frequency by about 400 cm^{-1}, whereas DVPT2 and CNEO-DFT predict a frequency very close to the experimental value.

DFT	DVPT2	CNEO-DFT	Expt.
3148 cm^{-1}	2788 cm^{-1}	2771 cm^{-1}	2750 cm^{-1}

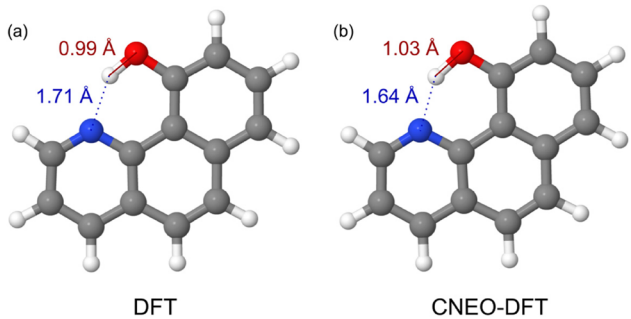


FIG. 2. Optimized geometry of HBQ obtained using (a) DFT and (b) CNEO-DFT. The O–H bond lengths and N···H hydrogen bond distances are indicated by the red solid lines and blue dotted lines, respectively.

To capture more complex anharmonic and mode coupling effects, we compute the IR spectra of HBQ from MD simulations. Experimental work has shown that the ν_{OH} band in the IR spectrum exhibits a distinctive finger-like structure appearing at ~2600 to 2900 cm^{-1}, as well as a peak at 3061 cm^{-1} assigned to aromatic C–H stretching modes.[24,26] The study by the Xiong group attributes the finger-like peak structure to anharmonic coupling of the fundamental ν_{OH} mode to four specific low-frequency modes: 265, 311, 414, and 508 cm^{-1}, identified using DFT-based anharmonic frequency analysis and a reduced-mode coupling Hamiltonian.[26] Here, we use CNEO-MD to reexamine the spectra and mode-specific couplings.

We performed CNEO-MD simulations at a series of elevated temperatures to progressively tune up the anharmonic coupling contributions [Fig. 3(a)].[47] We note that the simulation temperatures do not correspond directly to the experimental temperature (room temperature) but rather serve as a parameter used to incorporate anharmonic intermode couplings into classical MD simulations.[44] In particular, higher temperatures allow the system to explore farther from the equilibrium geometry, where anharmonic interactions between modes become more important, whereas lower temperatures restrict the motion to a nearly harmonic region of the PES with little anharmonic coupling. At 100 K, the spectrum closely resembles the harmonic result, with one intense ν_{OH} peak near 2771 cm^{-1}, corresponding to the ν_{OH} fundamental predicted by harmonic analysis. As the temperature increases, more features begin to appear and gradually gain intensity. Among all the simulated spectra, we observe that at 350 K, the CNEO-MD spectrum qualitatively reproduces the experimentally observed finger-like structure of the ν_{OH} band as well as the narrow aromatic C–H stretching band, although we note that the relative intensities of the ν_{OH} and aromatic C–H stretching bands are not quantitatively reproduced, and further increasing the simulation temperature is not likely to resolve this intensity discrepancy. The reason for this intensity disproportion remains unclear and warrants further investigation.

12 November 2026 14:28:20

Published under an exclusive license by AIP Publishing

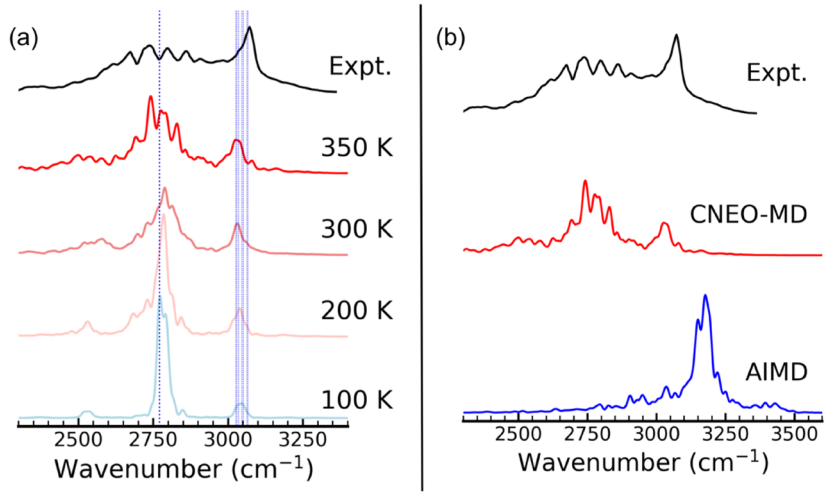


FIG. 3. IR spectra of HBQ obtained from MD simulations compared to the experimental spectrum digitized from the Fourier-transform IR spectrum of HBQ in CCl_4 at room temperature from Ref. 26. (a) IR spectra of HBQ obtained from CNEO-MD simulations at a series of temperatures (100, 200, 300, 350 K) compared with the experimental spectrum. Blue dotted lines indicate CNEO-DFT harmonic vibrational frequencies. (b) IR spectra of HBQ at 350 K calculated using CNEO-MD vs conventional AIMD. The CNEO-MD simulated spectrum reproduces the finger-like structure of the ν_{OH} band and captures the peak at 3061 cm^{-1}, which corresponds to aromatic C–H stretching modes.

Using the filter–reconstruction–projection analysis (see the supplementary material for more details),[47] we find evidence that the additional finger-like peaks may arise from the near-resonant mixing between the ν_{OH} fundamental and possible combination bands or overtones formed from mid-frequency (1000–1600 cm^{-1}) carbon backbone modes. Whereas in previous analyses we were able to propose a small number of dominant combination bands or overtones,[47] the complexity of the carbon backbone motions in HBQ gives rise to many possible candidates, so we cannot give a unique assignment here. Note that because CNEO-MD propagates its dynamics classically, the filter–reconstruction–projection analysis does not provide a direct quantum-mechanical assignment of combination bands or overtones, but it can suggest which vibrational motions may contribute to specific observed spectral features.[47]

Figure 3(b) compares the CNEO-MD spectrum to the conventional AIMD spectrum at 350 K. While AIMD also produces some subtle finger-like features, the ν_{OH} band is at a much higher frequency than in the experiment, which arises from the overestimation in conventional DFT harmonic analysis. This shift causes the O–H and aromatic C–H stretching regions to overlap, and the spectrum is far off from experiment.

C. Anharmonic vibrational mode coupling

1. Normal mode frequency shift analysis

Figure 4 presents the results of normal mode frequency shift analysis, which assesses the sensitivity of the ν_{OH} frequency to displacement along each individual normal mode. The modes are shown in order of increasing frequency, and only modes that induce

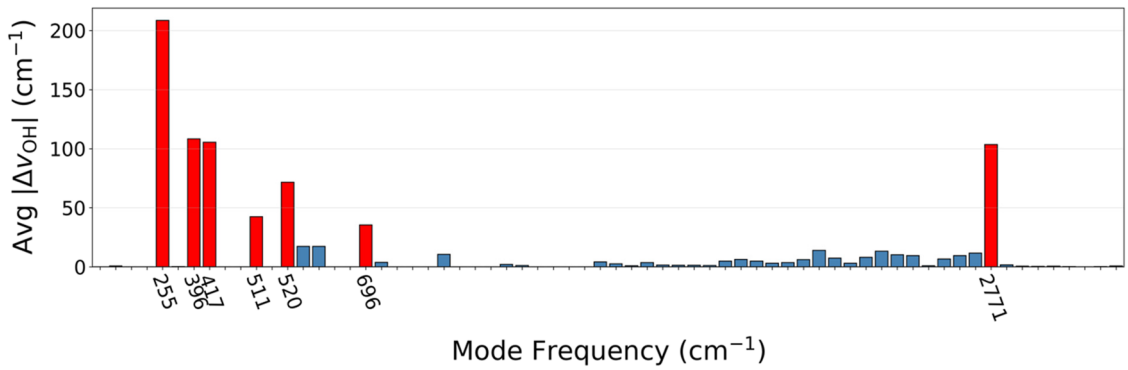


FIG. 4. Sensitivity of the ν_{OH} frequency to displacement along individual normal modes. Each bar represents the average magnitude change in the ν_{OH} frequency induced by displacing the optimized geometry along each normal mode in positive and negative directions with an amplitude corresponding to 300 K thermal energy, then recalculating the harmonic normal mode frequencies. Bars are arranged in order of increasing normal mode frequency along the horizontal axis; for clarity, only the frequencies of modes that produce significant changes in the ν_{OH} are labeled. Modes that induce significant changes in ν_{OH} frequency are highlighted in red. As expected, the ν_{OH} frequency is sensitive to its own displacement, shown by the bar at 2771 cm^{-1}. The 255 cm^{-1} mode produces the most significant shift in the ν_{OH} frequency, suggesting strong anharmonic coupling to the ν_{OH}. Five other low-frequency modes, specifically the 396, 417, 511, 520, and 696 cm^{-1} modes, also induce moderate changes in the ν_{OH} frequency. Most other modes produce only small frequency shifts, indicating weak or no coupling.

12 November 2026 14:28:20

Published under an exclusive license by AIP Publishing

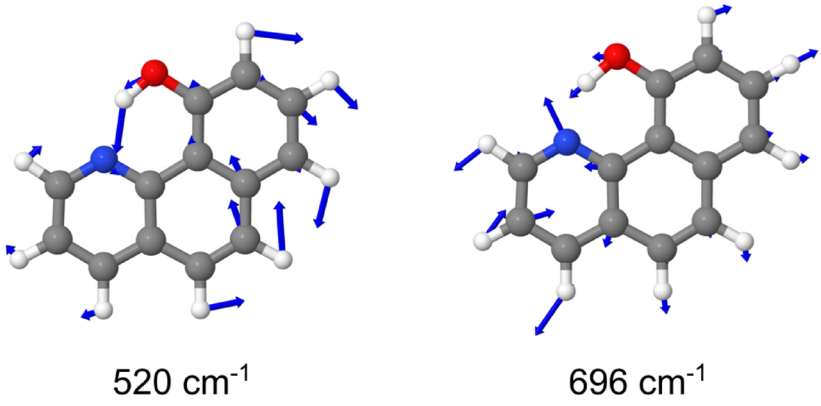


FIG. 5. Molecular motion of two newly identified coupled low-frequency modes: 520 and 696 cm^{-1}. Both are in-plane backbone bending motions that stretch and compress the hydrogen bond distance. See the supplementary material for all low-frequency mode motions.

notable shifts are labeled. Most modes induce negligible changes in ν_{OH} frequency, whereas a small number of low-frequency modes induce substantial shifts, indicating clear anharmonic coupling. The 255 cm^{-1} mode produces the largest frequency shift, demonstrating that it is strongly coupled to the ν_{OH}, and the 396, 417, 511, 520, and 696 cm^{-1} modes behave similarly. We observe that every mode that induces a moderate or significant change in the ν_{OH} frequency, aside from the ν_{OH} mode itself, is an in-plane backbone bending motion that modulates the oxygen–nitrogen distance, and thus the hydrogen bond distance. This observation is physically intuitive and consistent with previous understanding that changes in the donor–acceptor distance affect the hydrogen bond strength and, therefore, shift the ν_{OH} frequency.[84]

Compared to past investigations, we note that the 255 and 396 cm^{-1} modes correspond to the 242 and 386 cm^{-1} modes that have been identified experimentally as coupled to the ν_{OH}.[24–26] Furthermore, our results are also partially consistent with previous theoretical predictions from Cavazos and Xiong, who identified four low-frequency modes at 265, 311, 414, and 508 cm^{-1} as coupled to the ν_{OH}. Three of these modes—265, 414, and 508 cm^{-1}—align with our 255, 417, and 511 cm^{-1} modes, respectively, in both frequency and molecular motion. However, our results show no evidence of coupling to a mode near 311 cm^{-1} in either the normal mode frequency shift or electric field excitation analyses later (Sec. IV C 2). We additionally observe significant couplings from the 520 and 696 cm^{-1} modes (Fig. 5), which have not been previously identified to the best of our knowledge. A comprehensive list of relevant molecular motions is in the supplementary material.

2. CNEO-MD with electric field ν_{OH} excitation

To further validate the coupling, we perform real-time CNEO-MD by exciting the ν_{OH} mode with an electric pulse within CNEO-MD simulations and analyzing the intramolecular vibrational energy redistribution. A time-dependent oscillating electric field, polarized along the initial O–H bond and resonant with the ν_{OH} frequency, was multiplied by a Gaussian envelope to produce a finite-duration pulse that mimics the ultrafast pump excitation used in pump–probe spectroscopy experiments on HBQ. With this simulation, comparing vibrational energies before, during, and after excitation will reveal which modes gain energy as the ν_{OH} excites and decays and how this redistribution evolves over time.

In Fig. 6, the oscillation amplitudes of two representative modes are plotted. The amplitudes were obtained by projecting the CNEO-MD trajectory onto its corresponding normal mode basis, and these amplitudes are proportional to the square root of vibrational energy in the mode. The 255 cm^{-1} mode quickly gains energy upon ν_{OH} excitation and oscillates at its respective frequency, suggesting its coupling with the ν_{OH}. In contrast, the 880 cm^{-1} mode, although it is also an in-plane backbone bending mode and symmetry allows mode coupling, does not gain appreciable energy.

The six low-frequency modes that gain the most energy upon ν_{OH} excitation are the same six modes identified by normal mode frequency shift analysis; in particular, these are the 255, 396, 417, 511, 520, and 696 cm^{-1} modes. Among these, the 255 cm^{-1} mode gains the most energy in the simulations (see the

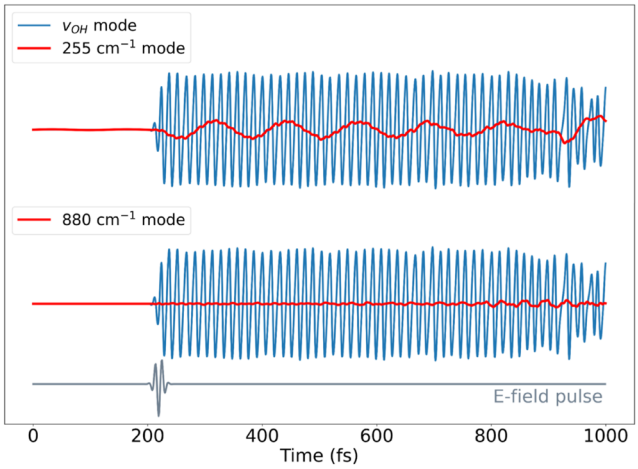


FIG. 6. Time evolution of the ν_{OH} (blue) and selected modes (red) during resonant excitation of the ν_{OH} within a CNEO-MD simulation. When the ν_{OH} mode is excited by the electric field pulse (gray) at time t = 200 fs, certain other modes gain amplitude. The mode coefficient's oscillatory amplitude is proportional to the square root of a mode's vibrational energy. For the representative modes shown above, the 255 cm^{-1} mode gains energy upon ν_{OH} excitation, whereas the 880 cm^{-1} mode does not gain appreciable energy. The supplementary material illustrates the mode coefficient decompositions for all low-frequency modes.

12 November 2026 14:28:20

Published under an exclusive license by AIP Publishing

supplementary material for all low-frequency mode decompositions) and also produces the largest ν_{OH} frequency shift in the normal mode frequency shift analysis. The remaining low-frequency modes show less energy gain and also smaller frequency shifts; for example, the 880 cm^{-1} mode has no clear increase in energy upon excitation.

The mid-frequency modes generally follow the same trend. Most of the modes from 700 to 1700 cm^{-1} gain less energy upon ν_{OH} excitation than the six low-frequency modes identified above and also produce smaller ν_{OH} normal mode frequency shifts. The C–H stretching modes near 3000 to 3100 cm^{-1} are an exception and do gain energy upon ν_{OH} excitation. However, this is because their frequencies are close to the ν_{OH}, and the short width of the pulse includes frequency components in the C–H stretch region, so they are directly excited by the pulse itself, rather than being coupled to the ν_{OH}.

V. CONCLUSIONS

In this work, we applied CNEO-DFT and CNEO-MD to study the vibrational spectrum and anharmonic couplings of the ν_{OH} in HBQ, an ESIPT molecule with a strong intramolecular hydrogen bond. We demonstrate that inclusion of NQEs is essential for accurate simulation of its vibrational spectrum. CNEO-DFT reduces the ν_{OH} frequency from the conventional DFT value of 3148 to 2771 cm^{-1}, quantitatively reproducing the experimental ~2750 cm^{-1}, and this improvement is robust across multiple functionals and basis sets. CNEO-MD simulations also reproduce the distinctive anharmonic finger-like structure of the ν_{OH} band. Filter–reconstruction–projection analysis suggests that these features arise from near-resonant mixing of the fundamental ν_{OH} with possible combination bands and overtones involving a dense set of mid-frequency modes.

Normal mode frequency shift analysis and electric-field CNEO-MD simulations consistently identify a set of low-frequency in-plane backbone bending modes that modulate the hydrogen bond distance as the dominant pathways for anharmonic coupling to the ν_{OH}. The 255 cm^{-1} mode exhibits the strongest coupling in both analyses, with additional significant coupling to the 396, 417, 511, 520, and 696 cm^{-1} modes. Notably, this is the first time that coupling to the 520 and 696 cm^{-1} modes has been identified, to the best of our knowledge. Together, these results establish that coupling to the ν_{OH} is distributed across several low-frequency in-plane backbone bending modes.

These findings provide a concrete understanding of the ground-state vibrational spectra and vibrational couplings that influence the ν_{OH} dynamics in HBQ and establish a foundation for future studies aimed at understanding and ultimately controlling ESIPT through mode-selective excitation or molecular design.

SUPPLEMENTARY MATERIAL

See the supplementary material for methodological details of mode coefficient decomposition, benchmarking of the ν_{OH} frequency using different functionals and basis sets with CNEO-DFT and conventional DFT (Table S1), convergence testing of the CNEO-MD IR spectrum with respect to the number of trajectories (Fig. S1), filter–reconstruction–projection analysis of the finger-like peaks of the ν_{OH} band (Fig. S2), visualizations of selected CNEO-DFT harmonic modes (Fig. S3), and mode coefficient decompositions of electric field CNEO-MD simulations (Fig. S4).

ACKNOWLEDGMENTS

H.K.N. acknowledges the support from the Gilbert Nathanson Student Support Summer Scholarship and the Hilldale Undergraduate/Faculty Research Fellowship. Y.W. acknowledges the support from the U.S. Department of Energy, Office of Science, Office of Advanced Scientific Computing Research, and Office of Basic Energy Sciences, through the Scientific Discovery through Advanced Computing (SciDAC) program under the NuQuantEm project at Pacific Northwest National Laboratory, under Grant No. FWP 85742, for the investigation of HBQ dynamics. Y.Y. acknowledges the funding support from the National Science Foundation under Grant No. 2238473 for the development and application of the CNEO framework. The authors acknowledge computing resources provided by the Center for High Throughput Computing at the University of Wisconsin–Madison.[85]

AUTHOR DECLARATIONS

Conflict of Interest

The authors have no conflicts to disclose.

Author Contributions

Hypatia K. Newton: Data curation (lead); Formal analysis (lead); Investigation (lead); Methodology (supporting); Writing – original draft (lead); Writing – review & editing (equal). **Yiwen Wang**: Conceptualization (supporting); Formal analysis (supporting); Investigation (supporting); Methodology (equal); Supervision (equal); Writing – original draft (supporting); Writing – review & editing (supporting). **Yang Yang**: Conceptualization (lead); Formal analysis (supporting); Funding acquisition (lead); Investigation (supporting); Methodology (equal); Supervision (equal); Writing – original draft (supporting); Writing – review & editing (equal).

DATA AVAILABILITY

The data that support the findings of this study are available within the article and its supplementary material.

REFERENCES

[1] H. C. Joshi and L. Antonov, "Excited-state intramolecular proton transfer: A short introductory review," Molecules **26**(5), 1475 (2021).
[2] D. McMorrow and M. Kasha, "Proton-transfer spectroscopy of 3-hydroxychromones. Extreme sensitivity to hydrogen-bonding perturbations," J. Am. Chem. Soc. **105**(15), 5133–5134 (1983).
[3] J. Jankowska and A. L. Sobolewski, "Modern theoretical approaches to modeling the excited-state intramolecular proton transfer: An overview," Molecules **26**(17), 5140 (2021).
[4] J. Zhao, S. Ji, Y. Chen, H. Guo, and P. Yang, "Excited state intramolecular proton transfer (ESIPT): From principal photophysics to the development of new

12 November 2026 14:28:20

Published under an exclusive license by AIP Publishing

chromophores and applications in fluorescent molecular probes and luminescent materials," Phys. Chem. Chem. Phys. **14**(25), 8803–8817 (2012).
[5]A. C. Sedgwick, L. Wu, H.-H. Han, S. D. Bull, X.-P. He, T. D. James, J. L. Sessler, B. Z. Tang, H. Tian, and J. Yoon, "Excited-state intramolecular proton-transfer (ESIPT) based fluorescence sensors and imaging agents," Chem. Soc. Rev. **47**(23), 8842–8880 (2018).
[6]J. E. Kwon and S. Y. Park, "Advanced organic optoelectronic materials: Harnessing excited-state intramolecular proton transfer (ESIPT) process," Adv. Mater. **23**(32), 3615–3642 (2011).
[7]P. Chonlateeroj, S. Arunlimsawat, P. Janthakit, R. Wannapakdee, W. Waengdongbung, T. Sudyoadsuk, P. Kumnorkaew, and V. Promarak, "Excited-state intramolecular proton transfer derivatives as self-absorption free luminophores for luminescent solar concentrators," Mater. Chem. Front. **9**(4), 695–709 (2025).
[8]S. Takeuchi and T. Tahara, "Coherent nuclear wavepacket motions in ultrafast excited-state intramolecular proton transfer: Sub-30-Fs resolved pump−probe absorption spectroscopy of 10-hydroxybenzo[h]quinoline in solution," J. Phys. Chem. A **109**(45), 10199–10207 (2005).
[9]M. Higashi and S. Saito, "Direct simulation of excited-state intramolecular proton transfer and vibrational coherence of 10-hydroxybenzo[h]quinoline in solution," J. Phys. Chem. Lett. **2**(18), 2366–2371 (2011).
[10]R. De Vivie-Riedle, V. De Waele, L. Kurtz, and E. Riedle, "Ultrafast excited-state proton transfer of 2-(2′-hydroxyphenyl)benzothiazole: Theoretical analysis of the skeletal deformations and the active vibrational modes," J. Phys. Chem. A **107**(49), 10591–10599 (2003).
[11]S. Lochbrunner, A. J. Wurzer, and E. Riedle, "Microscopic mechanism of ultrafast excited-state intramolecular proton transfer: A 30-Fs study of 2-(2′-hydroxyphenyl)benzothiazole," J. Phys. Chem. A **107**(49), 10580–10590 (2003).
[12]S. Biswas, J. W. Sandwisch, R. B. Weakly, and M. Khalil, "Tracking coherent vibronic and vibrational motions in ultrafast proton transfer," Nat. Commun. **17**(1), 6291 (2026).
[13]C. Schriever, M. Barbatti, K. Stock, A. J. A. Aquino, D. Tunega, S. Lochbrunner, E. Riedle, R. De Vivie-Riedle, and H. Lischka, "The interplay of skeletal deformations and ultrafast excited-state intramolecular proton transfer: Experimental and theoretical investigation of 10-hydroxybenzo[h]quinoline," Chem. Phys. **347**(1–3), 446–461 (2008).
[14]A. Gomez, A. Nimmrich, V. M. Freixas, C. Zhang, S. Mukamel, M. Khalil, and N. Govind, "Excited-state intramolecular proton transfer dynamics with neural network potentials and nuclear quantum effects," https://chemrxiv.org/doi/full/10.26434/chemrxiv.15003907/v3 (2026).
[15]P.-T. Chou, Y.-C. Chen, W.-S. Yu, Y.-H. Chou, C.-Y. Wei, and Y.-M. Cheng, "Excited-state intramolecular proton transfer in 10-hydroxybenzo[h]quinoline," J. Phys. Chem. A **105**(10), 1731–1740 (2001).
[16]P.-T. Chou and C.-Y. Wei, "Photophysics of 10-hydroxybenzo[*h*]quinoline in aqueous solution," J. Phys. Chem. **100**(42), 17059–17066 (1996).
[17]J. Lee, C. H. Kim, and T. Joo, "Active role of proton in excited state intramolecular proton transfer reaction," J. Phys. Chem. A **117**(7), 1400–1405 (2013).
[18]C. H. Kim and T. Joo, "Coherent excited state intramolecular proton transfer probed by time-resolved fluorescence," Phys. Chem. Chem. Phys. **11**(44), 10266 (2009).
[19]P. E. Hansen and J. Spanget-Larsen, "NMR and IR investigations of strong intramolecular hydrogen bonds," Molecules **22**(4), 552 (2017).
[20]K. B. Møller, R. Rey, and J. T. Hynes, "Hydrogen bond dynamics in water and ultrafast infrared spectroscopy: A theoretical study," J. Phys. Chem. A **108**(7), 1275–1289 (2004).
[21]K. Ohno, T. Shimoaka, N. Akai, and Y. Katsumoto, "Relationship between the broad OH stretching band of methanol and hydrogen-bonding patterns in the liquid phase," J. Phys. Chem. A **112**(32), 7342–7348 (2008).
[22]J. R. Lane, A. S. Hansen, K. Mackeprang, and H. G. Kjaergaard, "Kinetic energy density as a predictor of hydrogen-bonded OH-Stretching frequencies," J. Phys. Chem. A **121**(18), 3452–3460 (2017).
[23]B. T. Psciuk, M. Prémont-Schwarz, B. Koeppe, S. Keinan, D. Xiao, E. T. J. Nibbering, and V. S. Batista, "Correlating photoacidity to hydrogen-bond structure by using the local O–H stretching probe in hydrogen-bonded complexes of aromatic alcohols," J. Phys. Chem. A **119**(20), 4800–4812 (2015).
[24]M. Balasubramanian, A. Reynolds, T. J. Blair, and M. Khalil, "Probing ultrafast vibrational dynamics of intramolecular hydrogen bonds with broadband infrared pump-probe spectroscopy," Chem. Phys. **519**, 38–44 (2019).
[25]C. M. Loe, S. Chatterjee, R. B. Weakly, and M. Khalil, "Observing vibronic coupling in a strongly hydrogen bonded system with coherent multidimensional vibrational–electronic spectroscopy," J. Chem. Phys. **161**(17), 174203 (2024).
[26]A. Cavazos and W. Xiong, "Anharmonic coupling in a strong intramolecular H-bond system: Contributions to static and time-resolved vibrational spectra," J. Phys. Chem. Lett. **16**(51), 13199–13205 (2025).
[27]J. Kim, C. H. Kim, C. Burger, M. Park, M. F. Kling, D. E. Kim, and T. Joo, "Non-Born–Oppenheimer molecular dynamics observed by coherent nuclear wave packets," J. Phys. Chem. Lett. **11**(3), 755–761 (2020).
[28]T. E. Markland and M. Ceriotti, "Nuclear quantum effects enter the mainstream," Nat. Rev. Chem. **2**(3), 0109 (2018).
[29]S. M. Craig, F. S. Menges, C. H. Duong, J. K. Denton, L. R. Madison, A. B. McCoy, and M. A. Johnson, "Hidden role of intermolecular proton transfer in the anomalously diffuse vibrational spectrum of a trapped hydronium ion," Proc. Natl. Acad. Sci. U. S. A. **114**(24), E4706 (2017).
[30]N. Yang, C. H. Duong, P. J. Kelleher, A. B. McCoy, and M. A. Johnson, "Deconstructing water's diffuse OH stretching vibrational spectrum with cold clusters," Science **364**(6437), 275–278 (2019).
[31]H.-D. Meyer, U. Manthe, and L. S. Cederbaum, "The multi-configurational time-dependent hartree approach," Chem. Phys. Lett. **165**(1), 73–78 (1990).
[32]J. M. Bowman, "Self-consistent field energies and wavefunctions for coupled oscillators," J. Chem. Phys. **68**(2), 608–610 (1978).
[33]J. M. Bowman, "The self-consistent-field approach to polyatomic vibrations," Acc. Chem. Res. **19**(7), 202–208 (1986).
[34]S. Jang and G. A. Voth, "A derivation of centroid molecular dynamics and other approximate time evolution methods for path integral centroid variables," J. Chem. Phys. **111**(6), 2371–2384 (1999).
[35]I. R. Craig and D. E. Manolopoulos, "Quantum statistics and classical mechanics: Real time correlation functions from ring polymer molecular dynamics," J. Chem. Phys. **121**(8), 3368–3373 (2004).
[36]M. E. Tuckerman and A. Hughes, "Path integral molecular dynamics: A computational approach to quantum statistical mechanics," in *Classical and Quantum Dynamics in Condensed Phase Simulations* (World Scientific, Lerici Villa, Marigola, 1998), pp. 311–357.
[37]X. Xu and Y. Yang, "Constrained nuclear-electronic orbital density functional theory: Energy surfaces with nuclear quantum effects," J. Chem. Phys. **152**(8), 084107 (2020).
[38]X. Xu and Y. Yang, "Full-quantum descriptions of molecular systems from constrained nuclear–electronic orbital density functional theory," J. Chem. Phys. **153**(7), 074106 (2020).
[39]X. Xu and Y. Yang, "Molecular vibrational frequencies from analytic hessian of constrained nuclear–electronic orbital density functional theory," J. Chem. Phys. **154**(24), 244110 (2021).
[40]X. Xu, Z. Chen, and Y. Yang, "Molecular dynamics with constrained nuclear electronic orbital density functional theory: Accurate vibrational spectra from efficient incorporation of nuclear quantum effects," J. Am. Chem. Soc. **144**(9), 4039–4046 (2022).
[41]Z. Chen and Y. Yang, "The constrained nuclear–electronic orbital (CNEO) framework for nuclear quantum effects in quantum chemistry and molecular simulations," APL Comput. Phys. **2**(2), 020902 (2026).
[42]Z. Chen, J. Zheng, D. G. Truhlar, and Y. Yang, "Constrained nuclear-electronic orbital transition state theory using energy surfaces with nuclear quantum effects," J. Chem. Theory Comput. **21**(2), 590–604 (2025).
[43]Y. Zhang, Z. Liu, and Y. Yang, "Finite-temperature double proton transfer in formic acid dimer via constrained nuclear-electronic orbital molecular dynamics: Lower barriers and enhanced rates from nuclear quantum delocalization," J. Chem. Theory Comput. **21**(11), 5400–5408 (2025).
[44]Y. Zhang, Y. Wang, X. Xu, Z. Chen, and Y. Yang, "Vibrational spectra of highly anharmonic water clusters: Molecular dynamics and harmonic analysis revisited

12 November 2026 14:28:20

Published under an exclusive license by AIP Publishing

with constrained nuclear-electronic orbital methods," J. Chem. Theory Comput. **19**(24), 9358–9368 (2023).
[45]Y. Zhang, X. Xu, N. Yang, Z. Chen, and Y. Yang, "Describing proton transfer modes in shared proton systems with constrained nuclear–electronic orbital methods," J. Chem. Phys. **158**(23), 231101 (2023).
[46]J. Langford, Y. Zhang, Z. Chen, and Y. Yang, "Where is the hidden intramolecular H-bonding vibrational signal in the proline matrix IR spectrum?," J. Chem. Phys. **161**(13), 134302 (2024).
[47]Z. Liu, Y. Wang, Y. Zhang, N. Yang, and Y. Yang, "Characterizing infrared spectra of $OH^-\cdot(H_2O)_2$ and $OH^-\cdot(H_2O)_3$ with constrained nuclear-electronic orbital molecular dynamics," J. Phys. Chem. A **129**(43), 9883–9894 (2025).
[48]H. Chen, Y. Zhang, Y. Wang, K. Xuan, Z. Chen, and Y. Yang, "Analytic polarizability and vibrational Raman spectra from constrained nuclear-electronic orbital density functional theory," J. Chem. Phys. **163**(24), 244111 (2025).
[49]Z. Liu, Z. Chen, and Y. Yang, "Nonadiabatic dynamics with constrained nuclear-electronic orbital theory," J. Phys. Chem. Lett. **16**(25), 6559–6569 (2025).
[50]X. Xu, "Constrained nuclear-electronic orbital density functional theory with a dielectric continuum solvent model," J. Phys. Chem. A **127**(30), 6329–6334 (2023).
[51]X. Zhao, Z. Chen, and Y. Yang, "Constrained nuclear-electronic orbital QM/MM approach for simulating complex systems with quantum nuclear delocalization effects incorporated," Chem. Phys. Rev. **5**(4), 041401 (2024).
[52]Z. Chen and Y. Yang, "Periodic constrained nuclear-electronic orbital density functional theory for nuclear quantum effects: Method development and application to hydrogen adsorption on Pt(111)," J. Chem. Theory Comput. **21**(16), 7865–7877 (2025).
[53]S. Liu, J. Xu, and Y. Kanai, "Constrained nuclear–electronic orbital method for periodic density functional theory: Application to H_2 chemisorption on Si(001) surfaces," J. Chem. Phys. **163**(8), 084110 (2025).
[54]I. L. Thomas, "Protonic structure of molecules. I. Ammonia molecules," Phys. Rev. **185**(1), 90–94 (1969).
[55]J. F. Capitani, R. F. Nalewajski, and R. G. Parr, "Non-Born–Oppenheimer density functional theory of molecular systems," J. Chem. Phys. **76**(1), 568–573 (1982).
[56]T. Kreibich and E. K. U. Gross, "Multicomponent density-functional theory for electrons and nuclei," Phys. Rev. Lett. **86**(14), 2984–2987 (2001).
[57]H. Nakai, "Nuclear orbital plus molecular orbital theory: Simultaneous determination of nuclear and electronic wave functions without Born–Oppenheimer approximation," Int. J. Quantum Chem. **107**(14), 2849–2869 (2007).
[58]T. Ishimoto, M. Tachikawa, and U. Nagashima, "Review of multicomponent molecular orbital method for direct treatment of nuclear quantum effect," Int. J. Quantum Chem. **109**(12), 2677–2694 (2009).
[59]F. Pavošević, T. Culpitt, and S. Hammes-Schiffer, "Multicomponent quantum chemistry: Integrating electronic and nuclear quantum effects via the nuclear–electronic orbital method," Chem. Rev. **120**(9), 4222–4253 (2020).
[60]Z. Chen and Y. Yang, "Incorporating nuclear quantum effects in molecular dynamics with a constrained minimized energy surface," J. Phys. Chem. Lett. **14**(1), 279–286 (2023).
[61]Q. Sun, T. C. Berkelbach, N. S. Blunt, G. H. Booth, S. Guo, Z. Li, J. Liu, J. D. McClain, E. R. Sayfutyarova, S. Sharma, S. Wouters, and G. K. Chan, "PySCF: The python-based simulations of chemistry framework," WIREs Comput. Mol. Sci. **8**(1), e1340 (2018).
[62]Q. Sun, X. Zhang, S. Banerjee, P. Bao, M. Barbry, N. S. Blunt, N. A. Bogdanov, G. H. Booth, J. Chen, Z.-H. Cui, J. J. Eriksen, Y. Gao, S. Guo, J. Hermann, M. R. Hermes, K. Koh, P. Koval, S. Lehtola, Z. Li, J. Liu, N. Mardirossian, J. D. McClain, M. Motta, B. Mussard, H. Q. Pham, A. Pulkin, W. Purwanto, P. J. Robinson, E. Ronca, E. R. Sayfutyarova, M. Scheurer, H. F. Schurkus, J. E. T. Smith, C. Sun, S.-N. Sun, S. Upadhyay, L. K. Wagner, X. Wang, A. White, J. D. Whitfield, M. J. Williamson, S. Wouters, J. Yang, J. M. Yu, T. Zhu, T. C. Berkelbach, S. Sharma, A. Y. Sokolov, and G. K.-L. Chan, "Recent developments in the PySCF program package," J. Chem. Phys. **153**(2), 024109 (2020).
[63]Y. Yang (2026). "Theorychemyang/Pyscf," GitHub. https://github.com/theorychemyang/pyscf (accessed 22 June 2026).
[64]L.-P. Wang and C. Song, "Geometry optimization made simple with translation and rotation coordinates," J. Chem. Phys. **144**(21), 214108 (2016).
[65]A. Hjorth Larsen, J. Jørgen Mortensen, J. Blomqvist, I. E. Castelli, R. Christensen, M. Dułak, J. Friis, M. N. Groves, B. Hammer, C. Hargus, E. D. Hermes, P. C. Jennings, P. Bjerre Jensen, J. Kermode, J. R. Kitchin, E. Leonhard Kolsbjerg, J. Kubal, K. Kaasbjerg, S. Lysgaard, J. Bergmann Maronsson, T. Maxson, T. Olsen, L. Pastewka, A. Peterson, C. Rostgaard, J. Schiøtz, O. Schütt, M. Strange, K. S. Thygesen, T. Vegge, L. Vilhelmsen, M. Walter, Z. Zeng, and K. W. Jacobsen, "The atomic simulation environment—A python library for working with atoms," J. Phys.: Condens. Matter **29**(27), 273002 (2017).
[66]R. M. Hanson, "*Jmol*—A paradigm shift in crystallographic visualization," J. Appl. Crystallogr. **43**(5), 1250–1260 (2010).
[67]W. Humphrey, A. Dalke, and K. Schulten, "VMD: Visual molecular dynamics," J. Mol. Graphics **14**(1), 33–38 (1996).
[68]V. Barone, "Anharmonic vibrational properties by a fully automated second-order perturbative approach," J. Chem. Phys. **122**(1), 014108 (2005).
[69]J. Bloino and V. Barone, "A second-order perturbation theory route to vibrational averages and transition properties of molecules: General formulation and application to infrared and vibrational circular dichroism spectroscopies," J. Chem. Phys. **136**(12), 124108 (2012).
[70]M. J. Frisch, G. W. Trucks, H. B. Schlegel, G. E. Scuseria, M. A. Robb, J. R. Cheeseman, G. Scalmani, V. Barone, G. A. Petersson, H. Nakatsuji, X. Li, M. Caricato, A. V. Marenich, J. Bloino, B. G. Janesko, R. Gomperts, B. Mennucci, H. P. Hratchian, J. V. Ortiz, A. F. Izmaylov, J. L. Sonnenberg, D. Williams-Young, F. Ding, F. Lipparini, F. Egidi, J. Goings, B. Peng, A. Petrone, T. Henderson, D. Ranasinghe, V. G. Zakrzewski, J. Gao, N. Rega, G. Zheng, W. Liang, M. Hada, M. Ehara, K. Toyota, R. Fukuda, J. Hasegawa, M. Ishida, T. Nakajima, Y. Honda, O. Kitao, H. Nakai, T. Vreven, K. Throssell, J. A. Montgomery, Jr., J. E. Peralta, F. Ogliaro, M. J. Bearpark, J. J. Heyd, E. N. Brothers, K. N. Kudin, V. N. Staroverov, T. A. Keith, R. Kobayashi, J. Normand, K. Raghavachari, A. P. Rendell, J. C. Burant, S. S. Iyengar, J. Tomasi, M. Cossi, J. M. Millam, M. Klene, C. Adamo, R. Cammi, J. W. Ochterski, R. L. Martin, K. Morokuma, O. Farkas, J. B. Foresman, and D. J. Fox, *Gaussian16 Revision C.01*, Gaussian, Inc., Wallingford, CT, 2016.
[71]M. Piccardo, J. Bloino, and V. Barone, "Generalized vibrational perturbation theory for rotovibrational energies of linear, symmetric and asymmetric tops: Theory, approximations, and automated approaches to deal with medium-to-large molecular systems," Int. J. Quantum Chem. **115**(15), 948–982 (2015).
[72]A. D. Becke, "Density-functional thermochemistry. III. The role of exact exchange," J. Chem. Phys. **98**(7), 5648–5652 (1993).
[73]A. D. Becke, "Density-functional exchange-energy approximation with correct asymptotic behavior," Phys. Rev. A **38**(6), 3098–3100 (1988).
[74]C. Lee, W. Yang, and R. G. Parr, "Development of the Colle–Salvetti correlation-energy formula into a functional of the electron density," Phys. Rev. B **37**(2), 785–789 (1988).
[75]C. Adamo and V. Barone, "Toward reliable density functional methods without adjustable parameters: The PBE0 model," J. Chem. Phys. **110**(13), 6158–6170 (1999).
[76]N. Mardirossian and M. Head-Gordon, "ωB97M-V: A combinatorially optimized, range-separated hybrid, meta-GGA density functional with VV10 nonlocal correlation," J. Chem. Phys. **144**(21), 214110 (2016).
[77]F. Weigend and R. Ahlrichs, "Balanced basis sets of split valence, triple zeta valence and quadruple zeta valence quality for H to Rn: Design and assessment of accuracy," Phys. Chem. Chem. Phys. **7**(18), 3297 (2005).
[78]R. A. Kendall, T. H. Dunning, and R. J. Harrison, "Electron affinities of the first-row atoms revisited. Systematic basis sets and wave functions," J. Chem. Phys. **96**(9), 6796–6806 (1992).
[79]Q. Yu, F. Pavošević, and S. Hammes-Schiffer, "Development of nuclear basis sets for multicomponent quantum chemistry methods," J. Chem. Phys. **152**(24), 244123 (2020).
[80]Y. Yang, Y. Zhang, Y. Yang, and X. Xu, "Assessment of electron–proton correlation functionals for vibrational spectra of shared-proton systems by constrained

12 November 2026 14:28:20

Published under an exclusive license by AIP Publishing

nuclear-electronic orbital density functional theory," J. Chem. Phys. **161**(24), 244103 (2024).
[81]W. Schneider and W. Thiel, "Anharmonic force fields from analytic second derivatives: Method and application to methyl bromide," Chem. Phys. Lett. **157**(4), 367–373 (1989).
[82]U. Ahmed, M. P. Johansson, S. Lehtola, and D. Sundholm, "Density functional benchmark for quadruple hydrogen bonds," Phys. Chem. Chem. Phys. **27**(17), 8706–8718 (2025).
[83]N. Mardirossian and M. Head-Gordon, "Thirty years of density functional theory in computational chemistry: An overview and extensive assessment of 200 density functionals," Mol. Phys. **115**(19), 2315–2372 (2017).
[84]W. Mikenda, "Stretching frequency versus bond distance correlation of OD(H)· · ·Y (YN, O, S, Se, Cl, Br, I) hydrogen bonds in solid hydrates," J. Mol. Struct. **147**(1–2), 1–15 (1986).
[85]Center for High Throughput Computing, Center for High Throughput Computing, 2006, https://doi.org/10.21231/GNT1-HW21.

12 November 2026 14:28:20

Published under an exclusive license by AIP Publishing